High-impedance granular-aluminum ring resonators

Mahya Khorramshahi,[1,*] Martin Spiecker,[1,2] Patrick Paluch,[1,2] Simon Geisert,[1]
Nicolas Gosling,[1] Nicolas Zapata,[1] Lucas Brauch,[1] Christian Kübel,[3,4,5] Simone Dehm,[3]
Ralph Krupke,[1,3] Wolfgang Wernsdorfer,[1,2] Ioan M. Pop,[1,2,6] and Thomas Reisinger[1,†]

[1] *IQMT, Karlsruhe Institute of Technology, 76131 Karlsruhe, Germany*
[2] *PHI, Karlsruhe Institute of Technology, 76131 Karlsruhe, Germany*
[3] *INT, Karlsruhe Institute of Technology, 76131 Karlsruhe, Germany*
[4] *KNMFi, Karlsruhe Institute of Technology, 76131 Karlsruhe, Germany*
[5] *Department of Materials & Earth Sciences, Technische Universität Darmstadt, 64289 Darmstadt, Germany*
[6] *Physics Institute 1, Stuttgart University, 70569 Stuttgart, Germany*

(Received 22 February 2025; revised 6 June 2025; accepted 10 July 2025; published 27 August 2025)

Superconducting inductors with impedance surpassing the resistance quantum, i.e., superinductors, are important for quantum technologies because they enable the development of protected qubits, enhance coupling to systems with small electric dipole moments, and facilitate the study of phase-slip physics. We demonstrate superinductors with densely packed meandered traces of granular aluminum (grAl) with inductances up to 4 μH, achieving impedances exceeding 100 kΩ in the 4–8 GHz range. Ring resonators made with grAl meandered superinductors exhibit quality factors on the order of 10^5 in the single-photon regime, and low nonlinearity on the order of tens of hertz. Depending on the grAl resistivity, at 10 Hz, we measure frequency-noise spectral densities in the range of 10^2–10^3 Hz/$\sqrt{\text{Hz}}$. In some devices, in the single-photon regime, we observe a positive Kerr coefficient of unknown origin. Using more complex fabrication, the devices could be released from the substrate, either freestanding or suspended on a membrane, thereby further improving their impedance by a factor of 3.

DOI: 10.1103/n73t-7q1n

I. INTRODUCTION

In circuits with high characteristic impedance, Z_C, zero-point voltage fluctuations are enhanced [1,2], $V_{\mathrm{ZPF}} \propto \sqrt{Z_C}$, enabling coupling of superconducting microwave devices to other systems, e.g., phonons via direct piezoelectric coupling [3] or parametric electromechanical interactions [4], molecular qubits [5], as well as small electric dipoles and spins in quantum dots [2]. At the high end of Z_C, inductors with zero dc resistance and impedance exceeding the resistance quantum, $Z_C > R_Q = h/(2e)^2 \approx 6.45\,\mathrm{k\Omega}$, are known as superinductors [6,7]. They enable the realization of protected qubit architectures, such as fluxonium [8–14] and $0-\pi$ qubits [15–17], by delocalizing the wave function and mitigating flux noise. The high inductive reactance of superinductors is also essential for studying flux-tunneling-induced phase slips, facilitating the observation of dual Shapiro steps [18–20].

Long Josephson junction arrays are a widely used option for achieving high impedance with low loss [6,7], and their impedance can exceed hundreds of kΩ when suspended in vacuum [21,22]. However, these arrays—particularly in suspended configurations—are complex to fabricate and introduce unwanted nonlinearity [23]. Alternatively, geometric inductors optimized into suspended spiral shapes offer high linearity but remain challenging to fabricate [24,25].

Ideal superinductor technology would combine low dissipation, straightforward fabrication, and compatibility across diverse operational environments, including high magnetic fields, as required, for example, in spin [2], Andreev [26], or nanowire qubit devices [27–29].

In this context, disordered superconductors are particularly attractive because they can be densely patterned using standard lithographic techniques, while contributing substantial kinetic inductance, which dominates the total inductive response. Among the various candidate materials, several have been employed to fabricate devices exhibiting characteristic impedance, Z_C, higher than 1 kΩ and internal quality factors, Q_i, above 10^5 in

*Contact author: mahya.khorramshahi@kit.edu
†Contact author: thomas.reisinger@kit.edu

the single-photon regime. These include NbN [23,30,31], TiN [32–34], NbTiN [35–37], TiAlN [38], and granular aluminum (grAl) [10,39–42]. The associated self-Kerr nonlinearity can be tuned from approximately 10 to 10^5 Hz for both NbN [23,43] and TiN [44], and from 10^{-2} to 10^6 Hz for grAl [45,46]. In a recent study [47], the authors compared NbN and grAl devices, highlighting the following trade-off: NbN offers superior magnetic field resilience, which is beneficial for hybrid circuit quantum electrodynamics, while grAl is better suited to low-field regimes requiring high impedance and strong nonlinearity.

Here, we utilize grAl to explore the high-impedance frontier with meandered trace ring resonators. The meandering design is practical for achieving high impedance, as it allows for long inductive lines within a small area, maximizing inductance while minimizing capacitance [40]. We demonstrate ring resonators with impedance above 100 kΩ in the technologically relevant frequency range of 4–8 GHz. These resonators achieve quality factors around 10^5 in the single-photon regime, with nonlinearity in the tens of hertz. Frequency-noise spectral densities at 10 Hz range from 10^2–10^3 Hz/$\sqrt{\text{Hz}}$, depending on grAl resistivity.

II. RESONATOR DESIGN AND FABRICATION

grAl is a nanocomposite of Al grains in an aluminum oxide matrix [see Fig. 1(a)], forming a self-assembled three-dimensional network of Josephson junctions [see Fig. 1(b)]. It is superconducting for a wide range of normal-state resistivities, ρ, ranging from 1 to 10 000 μΩ cm [48], which can be adjusted via the oxygen partial pressure during deposition. This tunability enables precise control over its kinetic inductance, L_k, allowing the realization of inductors predominantly governed by kinetic inductance, with a kinetic inductance fraction, $\alpha = L_k/(L_k + L_g)$, approaching unity, where L_g is the geometric inductance.

The kinetic inductance, L_k, of a superconducting trace of width w and length ℓ is given by [49,50]

$$L_k = L_\square \frac{\ell}{w} = \frac{\hbar R_n}{\mathcal{C} k_B T_c \pi}\frac{\ell}{w}, \tag{1}$$

where $L_\square$ is the kinetic inductance per square, k_B is the Boltzmann constant, T_c is the superconducting critical temperature, and R_n is the normal-state sheet resistance. The superconducting gap is linked to the critical temperature by $\Delta(0) = \mathcal{C}\, k_B T_c$, with $\mathcal{C} = 1.76$ for grAl resistivity below 2 mΩ cm and $\mathcal{C} \approx 2.1$ for the high-resistivity range [48,52].

To increase the characteristic impedance of the resonator, $Z_C = \sqrt{L/C}$, where $L = L_k + L_g$ and C is the resonator's total capacitance, it is essential to optimize the resonator design to minimize C and maximize L. This is achieved by employing a meandered ring resonator [see Fig. 1(c)], where the capacitance is reduced by decreasing the ring's outer radius, r_{out}, and using the smallest possible meander pitch, p. Since α is close to unity, L is predominantly enhanced by increasing the kinetic inductance, L_k, through two mechanisms: increasing the number of squares in the trace, by increasing the length, ℓ, and reducing the width, w, of the resonator, and raising the sheet resistance, R_n, which can be achieved by using higher-resistivity films and by reducing film thickness.

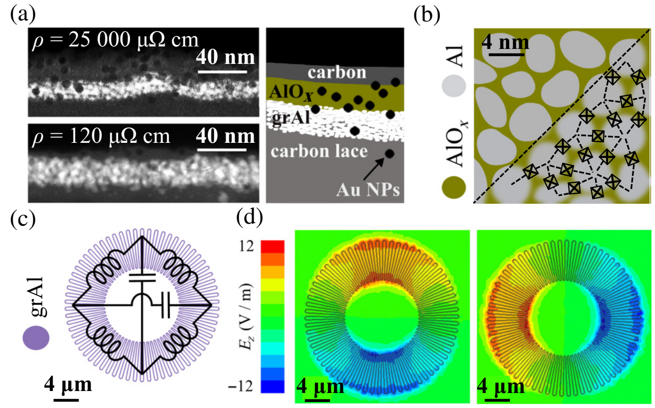

FIG. 1. Granular-aluminum (grAl) ring resonator design. (a) Energy-filtered transmission electron microscopy images of high-resistivity grAl (top, ≈25 000 μΩ cm) and low-resistivity grAl (bottom, ≈120 μΩcm). Energy filter at 15 eV highlights the aluminum volume plasmon. Viewing angle is tilted by 72° to the deposition direction for both images. Right-hand schematic is there to aid interpretation of the images. grAl was deposited on carbon lace visible at the bottom of the films. Dark particles are gold nanoparticles (Au NPs) introduced as fiducial markers for tracking the sample during rotation in tomography experiments. (b) Schematic of granular aluminum, illustrating aluminum grains (gray) encircled by aluminum oxide barriers. This microscopic configuration forms an effective array of Josephson junctions, which gives high kinetic inductance and tunable nonlinearity. (c) Design of the ring resonator and its equivalent circuit. Densely packed meander trace maximizes the ratio of inductance to self-capacitance. Resonator's symmetric design results in two degenerate modes, each involving one effective capacitor shunted by two parallel inductors. (d) Rendering of the electric field distribution to illustrate the charge distribution within the resonator. Modes are similar to dual modes in aluminum ring resonators in Ref. [51].

As shown in Fig. 1(d), when the ring is closed, the symmetric design of this distributed resonator results in two fundamental modes. The effective circuit model for each mode comprises a capacitor shunted by two parallel inductors, $L/4$.

The resonators are capacitively coupled to a common 50 Ω coplanar waveguide (CPW) for reflection measurements, as shown in Fig. 2. The entire structure is integrated within a silver ground plane, which suppresses parasitic modes and ensures a uniform magnetic field across the

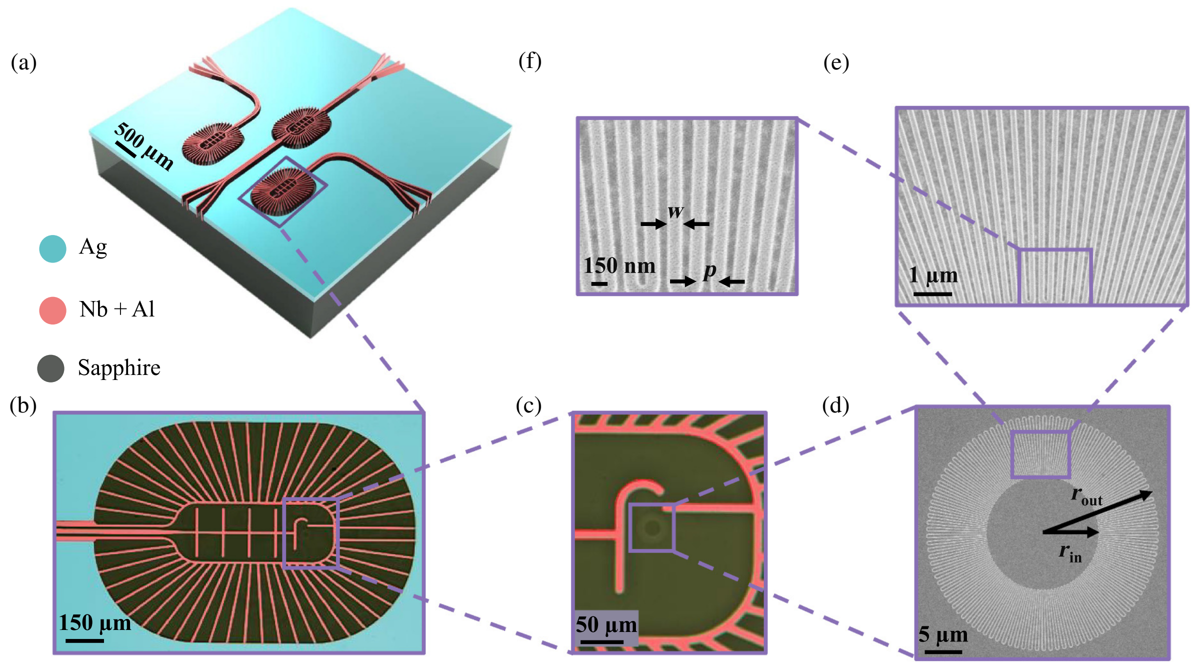

FIG. 2. Ring resonators in CPW architecture. (a) Three-dimensional rendering of the chip layout on a sapphire substrate featuring multiple CPWs, enabling the measurement of various devices, and a surrounding ground plane to suppress parasitic modes and ensure a uniform magnetic field. Ground plane mostly consists of silver, which avoids flux trapping and dampens microwave slot modes and phonons [53]. Central line of the CPW and the regions close to it consist of thin films of 15 nm niobium capped by 5 nm of aluminum. 5 nm Al capping layer is used to enable clean galvanic contact with the ground in overlapping regions, leveraging the argon milling recipe introduced and tested in Ref. [54]. (b) Optical false color image of the end section of the CPW coupled to several ring resonators. Central line splits into either rectangular coupling strips or (c) a semicircle at its end. Both the central line and the ground plane in this region consist of 10 μm wide superconducting strips of Nb + Al [see panel (a)], to minimize flux trapping. (d) Scanning electron microscope (SEM) image of a granular-aluminum ring resonator, highlighting the densely packed meander traces achieved through a single-step *e*-beam lithography process followed by lift-off. (e),(f) SEM images of the meandering lines at increasing magnification.

chip. Near the end of each CPW, we push the normal ground plane away from the central pin to reduce dissipation. In the proximity of the devices, the ground plane consists of narrow superconducting lines connected to the normal plane; this avoids the creation of superconducting loops and associated flux trapping. The configuration of the end of the CPW feed line enables flexible coupling to the small rings. It intentionally creates different coupling strengths for the two modes, thereby breaking the symmetry and lifting the degeneracy of the two fundamental modes. Positioning the ring near the semicircular structure at the end of the feed line [see Fig. 2(c)] results in strong coupling for both modes, while placing it within a square structure visible in the center of Fig. 2(b) leads to uneven coupling of the modes to the feed line. The compact design allows for the integration of three separate CPW sets on a single chip, each isolated by the ground plane, enabling the measurement of multiple ring resonators with varying design parameters.

The rings are patterned using a single-step electron-beam lithography process followed by lift-off on a *c*-plane sapphire substrate with zero-angle evaporation deposition. See Figs. 2(d)–2(f) for images of one of the fabricated rings. The pitch values, p, range from 200 to 520 nm, with widths, w, between 150 and 170 nm, and film thicknesses, t, from 20 to 30 nm. We wire-bond each chip to a copper housing that is surrounded by magnetic- and infrared-radiation-shielding barrels made of copper/aluminum and mu-metal (see Appendix A). The assembly is connected to the mixing chamber (MXC) stage of a dilution cryostat, operating at approximately 20 mK.

III. RESULTS AND DISCUSSION

In Fig. 3(a), we show a typical phase response of a ring resonator in a microwave-reflection measurement. The two fundamental modes are clearly visible, separated by approximately 25 MHz, with their respective coupling quality factors, Q_c, differing by approximately a factor of 4.

A summary of the measured fundamental mode frequencies for nine resonators is shown in Fig. 3(b), for grAl resistivities between 800 and 2500 μΩcm. By performing finite-element simulations for rings with varying ℓ and matching the simulated frequencies with measurements, we deduce the inductance per square for each grAl film, ranging from 180 to 670 pH/sq ($L_\square$).

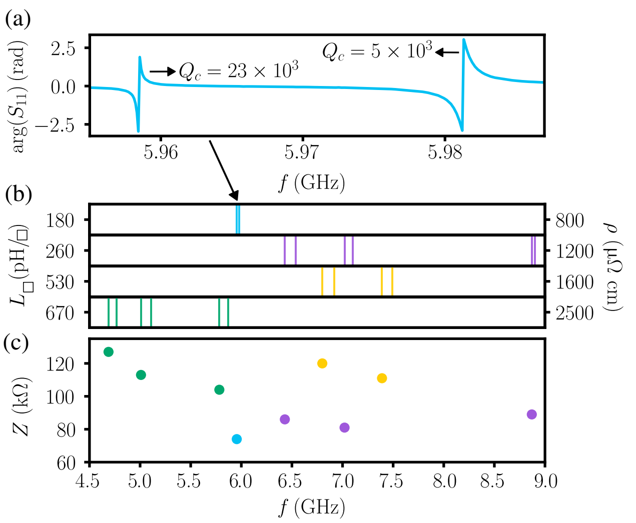

FIG. 3. Frequency and impedance of granular-aluminum superinductors. (a) Graph shows the phase response of one of the doublet ring resonances with frequency separations of approximately 25 MHz, pointing to the asymmetry due to the difference in coupling capacitance of the two modes and fabrication imperfections. (b) Frequency spectra of the fabricated and measured granular-aluminum ring resonators. Each row corresponds to an inductance per square and the corresponding resistivity, as determined from Eq. (1). (c) Graph determines the impedance of each ring resonator up to the first fundamental mode. Filled circular markers represent the measured impedance of the fabricated and characterized rings, with the highest impedance recorded at 127 kΩ at a resonant frequency of 4.6 GHz. These values are obtained using $Z = 2\pi f_0 L$.

We determine the impedance up to the first fundamental mode, f_0, from $Z = 2\pi f_0 L$, where L denotes the inductance of the entire ring [21,24], as summarized in Fig. 3(c). The highest impedance, 127 kΩ, was achieved for a ring with a sheet inductance of 670 pH/sq, and specific dimensions of 325 nm pitch, $r_{\mathrm{in}} = 6.7\,\mu$m, $r_{\mathrm{out}} = 2r_{\mathrm{in}}$, and 20 nm thick. A detailed summary of all measured devices is provided in Table I in Appendix B.

In a simplified model (see Appendix C), we find that the impedance and lowest-mode frequency scale with the layout parameters and sheet inductance as follows:

$$Z \propto \sqrt{\frac{r_{\mathrm{in}} L_\square}{pw}}, \quad f_0 \propto \sqrt{\frac{pw}{r_{\mathrm{in}}^3 L_\square}}. \tag{2}$$

Indeed, as shown in Fig. 4(a), the impedance for our measured resonators follows this scaling. Notably, $Zf_0 \propto 1/r_{\mathrm{in}}$, as illustrated in Fig. 4(b), which means that, to maximize the impedance at a given frequency, we need to minimize r_{in} and compensate for the resulting change in frequency by decreasing the ratio of $pw/L_\square$. The lowest-achievable value for the ratio of $pw/L_\square$ depends on the grAl material's properties and the finesse of the lithography process. The maximum value for $L_\square$ is limited by the resistivity

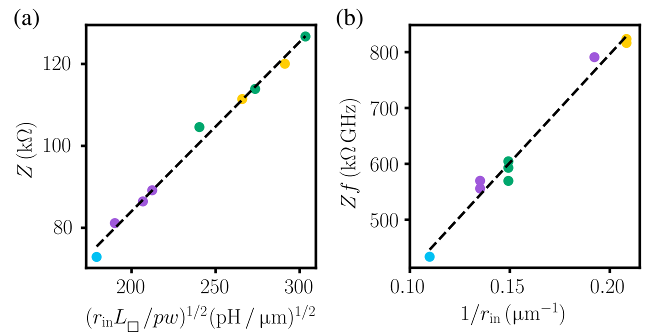

FIG. 4. Measured impedance scaling with geometry and resistivity. Plot of measured Z (a) and Zf (b) as a function of $(r_{\mathrm{in}} L_\square/pw)^{1/2}$ and $1/r_{\mathrm{in}}$, respectively, confirming their linear dependence (cf. dashed lines), consistent with Eq. (2). Color code in both panels is consistent with Fig. 3. Details for each resonator are given in Table I.

threshold for the grAl superconducting-to-insulating transition [48,52], in the range of 10 mΩcm, and by the thinnest continuous and stable films. For grAl films below 20 nm, we observe significant fluctuations in their resistivity between different cooldowns, indicating that structural inhomogeneities and instabilities play a dominant role. We found that devices with $w \geq 150$ nm always resulted in stable devices, which was not the case for $w \approx 60$ nm, likely due to inhomogeneities in the wires [see Fig. 1(a)]. The smallest pitch we could achieve with our current electron-beam lithography process was 200 nm (see Appendix D). Taking these considerations into account, we believe that a fine-tuned optimal grAl device operational in the 4–8 GHz range can reach impedance values in the range of 200 kΩ (see Appendix E) on silicon or sapphire substrates, and this value can be increased by a factor of approximately 3, to exceed 0.5 MΩ for suspended devices.

We calculate the noise spectral density, $S(f)$, by monitoring the resonant frequency over time and applying the method used in Ref. [55]. As shown in Fig. 5(a), the low-frequency noise exhibits a $1/f$ dependence. We note that $S(f)$ evaluated at a frequency of 10 Hz is observed in the range of 200–1000 Hz/$\sqrt{\mathrm{Hz}}$, which is 1–2 orders of magnitude larger than that for grAl resonators of similar thickness and resistivity but lower impedance [56]. In addition, these values are 2 orders of magnitude larger than those of aluminum resonators [57]. The frequency-independent noise component at high frequency (white noise), modeled by a constant amplitude, S_0, is due to the measurement setup. It is nearly negligible in our data. To model the low-frequency noise, we use $S_{1/f} \propto f^{-\alpha}$, where $\alpha \approx 1$. Fitting this model to the measurements shown in Fig. 5(a), α ranges from approximately 0.8 to 0.97, which could be due to contributions from other noise sources. Note that the three data sets with the highest resistivity exhibit visible deviations from pure $S(f)$ dependence, which is compatible with an added Lorentzian component.

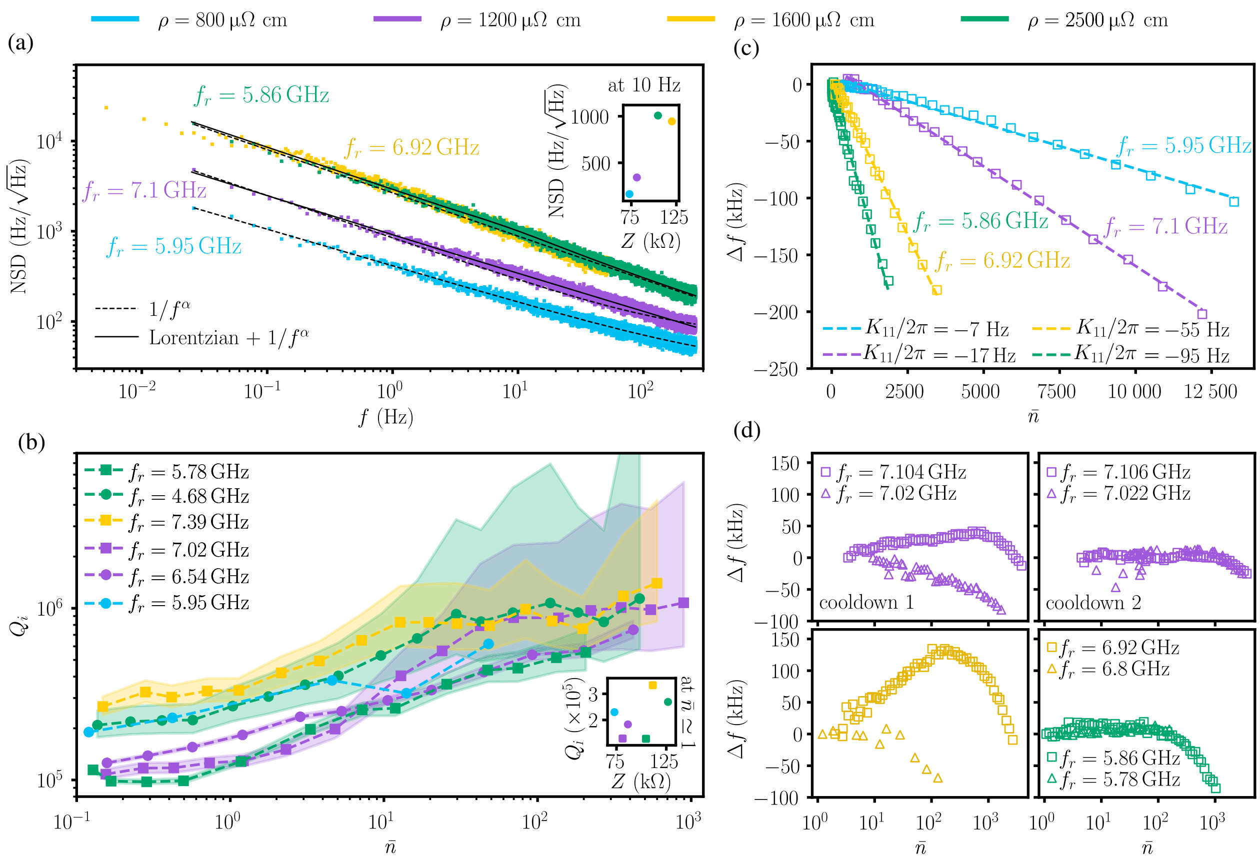

FIG. 5. Resonator performance. (a) Noise spectral density, $S(f)$, as a function of frequency, f, for grAl resonators. Spectra were computed from time traces and are shown for four different resistivity values. Data fit the model $S(f) = S_0 + S_1/f^{\alpha}$, with α ranging from 0.8 to 0.97. Two curves corresponding to resistivity values of $\rho = 2500\,\mu\Omega\,\text{cm}$ and $\rho = 1200\,\mu\Omega\,\text{cm}$ are plotted in green and purple, respectively; these exhibit behavior that is better described by a Lorentzian model combined with a $1/f^{\alpha}$ dependence at higher frequencies. Inset displays the impedance values corresponding to the frequency-noise spectral densities measured at 10 Hz. (b) Intrinsic quality factors, Q_i, plotted against average photon numbers in the granular-aluminum resonators up to the bifurcation threshold, $\bar{n}_{\text{max}}$. Average number of photons is given by $\bar{n} = 2Q_c P_{\text{cold}}/\omega_0^2$, where P_{cold} is the incident microwave power at the device [61]. Shaded intervals indicate the uncertainty range due to Fano interference [60]. For better visibility, we do not show this uncertainty range for the data set in blue, as it approximately corresponds to an order of magnitude. Inset presents impedance values derived from single-photon Q_i measurements. (c) Shift in resonance frequency as a function of average photon number for four different rings with varying resistivity is shown. Self-Kerr coefficient, K_{11}, was determined by fitting the frequency shift data to a linear model. Higher-resistivity grAl samples exhibit higher K_{11}, consistent with theoretical expectations that K_{11} is proportional to ρ/V, where ρ is resistivity and V is the volume [45]. (d) Anomalous shifts in resonance frequency with photon number. In some ring resonators, we observe an exponential shift to higher frequency at low photon numbers. In the top-two panels, purple data points show the two modes of the same ring resonator measured during two different cooldowns. In the first, we observe the exponential shift to a higher frequency for the higher-frequency mode, while the lower-frequency mode almost symmetrically shifts, but to a lower frequency. This occurs before the usual Kerr nonlinearity at higher photon numbers documented in (c). In the second cooldown, the exponential shifts are no longer observed. In the bottom-left panel, a similar anomalous shift is observed for a resonator with higher-resistivity grAl. Next to it, we show an example of a high-resistivity grAl resonator that does not show this anomalous shift.

This suggests the presence of random telegraph noise, which decays exponentially over a characteristic timescale given by the position of the peak in the noise spectrum [58]. Note that, in our case, the peak is less pronounced than that in Ref. [59].

To evaluate loss in the resonators, we measure the complex S_{11} signal and extract the internal quality factor, Q_i, and the coupling quality factor, Q_c, using the method in Ref. [60]. To minimize Fano-interference systematic errors, we design Q_c comparable to Q_i. In Fig. 5(b), we plot the fitted Q_i values as a function of photon number, $\bar{n}$. In the single-photon regime, Q_i is on the order of 10^5 and appears independent of resistivity and impedance. The value aligns with previous results for granular-aluminum resonators made using similar processes [61]. Since the participation ratio in the compact resonators presented here is larger, this suggests that, within the explored range, surface dielectric losses are not dominant. In Ref. [42], it was demonstrated that by optimizing the fabrication process and using thicker layers at similar resistivities, but lower impedance, quality factors above 10^6 could be achieved. These low levels of loss make high-impedance grAl resonators appealing for superconducting quantum circuits. At higher power levels, Q_i saturates to values close to 10^6, indicating that the dominant loss mechanism, potentially dielectric loss [62,63] or quasiparticle bursts [64,65], is saturable, as commonly observed for other superconducting materials.

In Fig. 5(c), we show that the resonators are comparatively linear, considering their high impedance. We determine the Kerr coefficient, K_{11}, which quantifies the frequency shift of the fundamental mode with the addition of one photon, by performing a linear fit to the frequency shift as a function of $\bar{n}$ in the high-photon-number regime. Our measurements indicate that K_{11} is in the range of tens of hertz. As seen in Fig. 5(c), resonators with higher resistivity and thinner films exhibit larger K_{11} values compared to those with lower resistivity and thicker films. This is consistent with modeling grAl as a one-dimensional array of Josephson junctions [45]; in that case, we expect $K_{11} \propto \rho/V$, where V is the resonator current mode volume.

An intriguing aspect of our measurements is the observation of a positive frequency shift as a function of photon number in some resonators, as shown in Fig. 5(d). We observe that the frequency initially increases at very low photon numbers before the drop corresponding to the Kerr nonlinearity discussed in the previous paragraph. Some ring resonators exhibit this effect, while others do not, and we cannot identify a correlation of this effect with resistivity, impedance, or other device parameters. Additionally, this positive frequency shift versus $\bar{n}$ can vary for the same device between cooldowns. Similar observations were recently reported on resonators integrating a flake of van der Waals cuprate superconductor [66]. This behavior is highly relevant for quantum devices operating in the low-power regime, and it needs further investigation to fully understand its underlying mechanisms, possibly related to strongly coupled spurious two-level systems [67–69].

IV. CONCLUSION

We fabricated and characterized granular-aluminum meandered trace ring resonators, achieving high impedance with a single-step lift-off *e*-beam lithography process. We propose a model in which the impedance and frequency of grAl resonators scale predictably with design parameters, with maximal impedance achieved by minimizing the diameter and correspondingly adjusting the pitch, trace width, and sheet inductance, within material and lithographic constraints. Our best devices exhibit kinetic inductances up to 4 μH and impedances exceeding 100 kΩ, about 16 times the resistance quantum. We demonstrated quality factors on the order of 10^5 in the single-photon regime, making them suitable for quantum information processing. Their measured self-Kerr nonlinearity, in the range of tens of hertz, is significantly lower than in Josephson junction arrays. Interestingly, we observe an anomalous positive frequency shift at low photon numbers of unknown origin. Further impedance enhancements could be achieved by reducing the dielectric constant, for example, through backside etching or by detaching from the substrate.

ACKNOWLEDGMENTS

We are grateful to L. Radtke and S. Diewald for technical assistance. We thank Mathieu Fechant, Horst Hahn, David Niepce, Dennis Rieger, and Patrick Winkel for constructive discussions and feedback. We acknowledge funding from the European Union's Horizon 2020 research and innovation program under Marie Skłodowska-Curie Grant Agreement No. 847471 (QUSTEC) and the Federal Ministry of Education and Research [Projects QSolid (FKZ: 13N16151) and GeQCoS (FKZ: 13N15683)]. The use of facilities was supported by the KIT Nanostructure Service Laboratory (NSL) and the Karlsruhe Nano Micro Facility (KNMFi). We acknowledge qKit for providing a convenient measurement software framework.

DATA AVAILABILITY

The data that support the findings of this article are openly available [70].

APPENDIX A: SETUP

As shown in Fig. 6, each chip's CPW is aluminum wirebonded to a 50 Ω transmission line, with the ground plane bonded to a nonmagnetic oxygen-free high-conductivity copper box to minimize spurious modes. This box features a tightly screwed lid to prevent radiation leakage. The entire assembly is mounted on a copper rod attached to the MXC stage of a dilution cryostat and enclosed within a series of magnetic shields, similar to the setup in Ref. [54], including a Cu/Al bilayer and an additional mu-metal shield to ensure effective magnetic shielding.

The input signal, generated by a vector network analyzer (VNA), is transmitted through cables, with attenuators at various cryogenic stages, as detailed in Fig. 6. For single-port reflection measurements, a cryogenic circulator separates the input and output signals. The reflected output signal then passes through a two-stage isolator, which shields against 4 K stage radiation, and through a low-pass filter before reaching a low-noise high-electron-mobility transistor (HEMT) amplifier via NbTi cables with minimal noise contribution. Finally, the amplified signal is sent to commercial room-temperature amplifiers and then back to the VNA output.

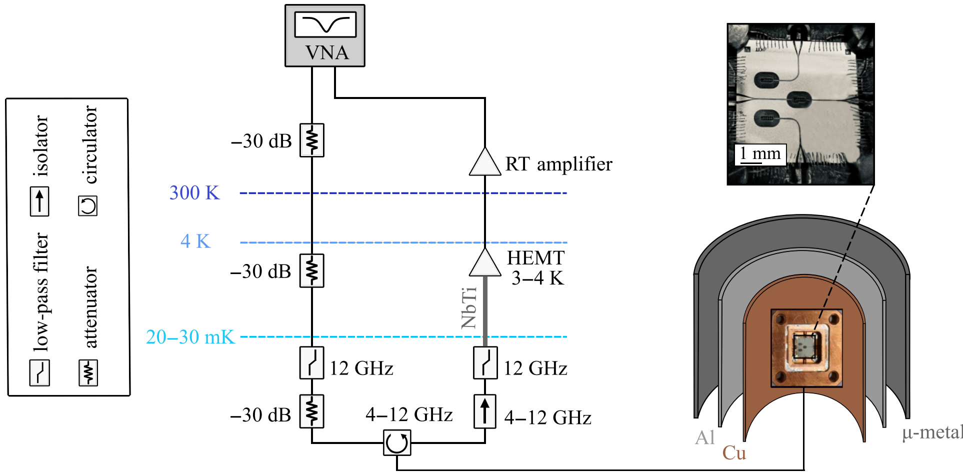

FIG. 6. Experimental setup. Measurement setup comprises a sample box housing the device under test, which is enclosed within a multilayer magnetic shield to ensure effective isolation. Input signal from a VNA is transmitted through coaxial cables with attenuation applied at each thermal stage of the dilution cryostat before reaching the sample at the 20–30 mK MXC stage. Reflection measurements are performed by using a cryogenic circulator to separate input and output signals. Reflected signal is subsequently amplified by a HEMT amplifier at the 4 K stage and a room-temperature amplifier before being returned to the VNA. Dashed lines in the schematic indicate thermalization stages and a legend explains the symbols used to represent components such as circulators, isolators, attenuators, and amplifiers in the setup.

APPENDIX B: DESIGNED AND EMPIRICALLY EXTRACTED PARAMETERS

We confirmed the accuracy of geometric parameters via SEM imaging. The resonance frequency, f_0, was measured experimentally, as detailed in Appendix A. $L_\square$ was determined by fitting measured f_0 to simulated frequencies based on nominal design parameters.

The total inductance, L, was calculated based on geometric parameters and $L_\square$, using $L = l/w \times L_\square$, where

TABLE I. Summary of ring resonator parameters, including geometrical dimensions, $L_\square$, Z, and f_0 extracted from both measurements and simulations. Q_c was determined using the circle-fit method. This table outlines the key design parameters influencing resonator performance, providing a basis for optimization in various applications.

Resonator	r_{in} (μm)	w (nm)	l (μm)	p (nm)	t (nm)	f_0 (GHz)	$L_\square$ (pH/□)	L (μH)	C (fF)	Z (kΩ)	Q_c ($\times 10^3$)
1	9.1	170	1849	300	30	5.95	180	1.95	1.46	72.9	23
2	9.1	170	1849	300	30	5.98	180	1.95	1.45	72.9	5
3	7.4	150	1239	300	30	6.43	260	2.14	1.14	86.45	5
4	7.4	150	1239	300	30	6.54	260	2.14	1.10	86.45	600
5	7.4	150	1066	355	30	7.02	260	1.84	1.11	81.15	150
6	7.4	150	1066	355	30	7.10	260	1.84	1.09	81.15	20
7	5.2	150	928	200	30	8.87	260	1.60	0.80	89.17	25
8	5.2	150	928	200	30	8.9	260	1.60	0.79	89.17	22
9	4.8	150	796	200	20	6.80	530	2.81	0.78	120.05	50
10	4.8	150	796	200	20	6.92	530	2.81	0.75	120.05	30
11	4.8	150	681	240	20	7.39	530	2.40	0.77	111.43	230
12	4.8	150	681	240	20	7.49	530	2.40	0.75	111.43	130
13	5.6	150	875	300	20	5.70	600	3.50	0.89	125.35	200
14	5.6	150	875	300	20	5.81	600	3.50	0.85	125.35	130
15	5.6	150	741	253	20	6.03	600	2.96	0.94	112.14	60
16	5.6	150	741	253	20	6.13	600	2.96	0.91	112.14	6
17	6.7	150	966	325	20	4.68	670	4.31	1.07	126.7	140
18	6.7	150	966	325	20	4.76	670	4.31	1.03	126.7	50
19	6.7	150	806	400	20	5.00	670	3.60	1.12	113.9	8
20	6.7	150	806	400	20	5.11	670	3.60	1.07	113.09	6
21	6.7	150	646	518	20	5.78	670	2.88	1.05	104.59	260
22	6.7	150	646	518	20	5.86	670	2.88	1.02	104.59	30

l/w represents the number of squares. ρ was calculated using Eq. (1), with the critical temperature, T_c, set to approximately 2.2 K for the calculation.

Z was derived from $Z = 2\pi f_0 L$, assuming that the entire ring behaved as an inductor up to the resonance frequency. Q_i and Q_c were both extracted using the circle-fit method. The value of Q_c is influenced by the ring's position relative to the feed line, as well as the ring's radius—the smaller the radius, the weaker the coupling.

A summary of all parameters discussed above is given in Table I.

APPENDIX C: MODEL OF RING SUPERINDUCTORS

Ignoring the turns, which are approximately equal to the sum of πr_{in} and πr_{out}, the inductance can be approximated as $L = N L_\square r_{\text{in}}/w$. As we can see in Fig. 7(a), w is the wire width, $L_\square$ is the inductance per square, and r_{in} is the inner radius of the ring. The outer radius, r_{out}, is related to the inner radius by $r_{\text{out}} = 2r_{\text{in}}$. Here, N is the number of meanders, which is proportional to $2\pi r_{\text{in}}/p$, where p is the pitch (the sum of wire width and spacing). Substituting this relationship, we find

$$L \propto \frac{r_{\text{in}}^2 L_\square}{pw}.$$

The capacitance, C, of the ring resembles that of a coplanar capacitor composed of two square plates with sides r_{in} and separated by a length of $2r_{\text{in}}$. The capacitance of such a capacitor scales linearly with the plate width, and thus, r_{in}. Therefore, we can approximate the ring capacitance as $C \propto r_{\text{in}}$ [71].

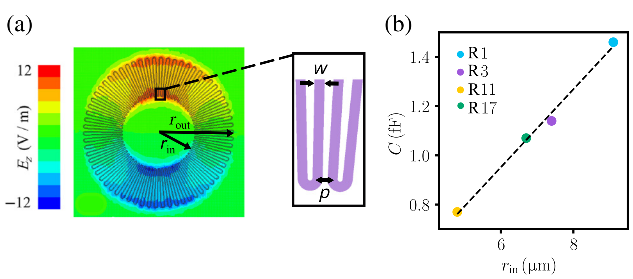

FIG. 7. Geometric design and capacitance scaling in ring superinductors. (a) Electric field distribution of the ring superinductor, highlighting the capacitor plates and remaining sections of the ring acting as inductors. We define r_{in} and r_{out} of the ring resonator as indicated. Magnified plot illustrates how we define w and p. (b) Capacitance as a function of r_{in} for rings with varying inductance per square and resistivity. Each data point corresponds to a specific resonator, with details listed in Table I. Dashed line acts as a guide to the eye and confirms the linear dependence of capacitance on r_{in} for the range of design parameters used here.

In Fig. 7(b), we confirm that this linear dependency is consistent with the capacitances determined from HFSS.

The resonance frequency is derived from the two expressions for L and C using the harmonic oscillator equation:

$$f_0 \propto \frac{1}{\sqrt{LC}} \propto \sqrt{\frac{pw}{r_{\text{in}}^3 L_\square}}.$$

The impedance, Z, depends on both the inductance and capacitance of the ring and can be expressed again using the expressions for L and C determined above:

$$Z \propto \sqrt{\frac{r_{\text{in}} L_\square}{pw}}.$$

Again, we confirm this proportionality of Z to the design parameters for the resonators listed in Table I in the plot shown in Fig. 4(a). In addition, we confirm in Fig. 4(b)

TABLE II. Summary of fabrication details for the ring resonators, including resist spinning, *e*-beam lithography for patterning, plasma cleaning, and grAl deposition in a dynamic oxygen environment. The resistivity of the resulting grAl films ranges from 800 to 2500 μΩ cm.

Resist coating	
Substrate	*c*-Plane sapphire
e-Beam resist	PMMA A4 (thickness = 200 nm)
Acceleration	1000 rpm s^{-1}
Spread cycle	300 rpm for 4 s
Spin speed	5000 rpm for 60 s
Baking temperature	150 °C for 3 min
Conductive coating	Electra 92 (AR-PC 5090)
Acceleration	1000 rpm s^{-1}
Spread cycle	500 rpm for 1 s
Spin speed	2000 rpm for 60 s
Baking temperature	85 °C for 2 min
***e*-Beam exposure**	
Acceleration voltage	50 kV
Beam current	100 pA
Step size	10 nm
Development	
Conductive-coating removal	Water (RT) for 30 s
Developer	MIBK 1 : 3 IPA at 0 °C for 30 s
Deposition process	
Plasma cleaning	
Mass flows	O_2/Ar (10 sccm/5 sccm)
Beam parameters	$U_{\text{beam}} = 200$ V, $I_{\text{beam}} = 10$ mA
Gettering	
Ti evaporation rate	0.2 nm s^{-1} for 2 min
grAl deposition	
Al evaporation rate	1 nm s^{-1}
O_2 pressure	10^{-5}–10^{-4} mbar

that the product Zf_0 only depends on the ring radius. This shows that, for a given fixed frequency, the impedance can be increased (maximizing the product) only by reducing the radius and compensating for the associated frequency shift with one of the other design parameters (p, w, or $L_\square$). This compensation does not affect the product Zf_0.

APPENDIX D: FABRICATION

The device being tested includes the ring resonators, CPW, and ground plane. It is fabricated on a double-polished 2 inch *c*-plane sapphire wafer with a thickness of 330 µm. The lift-off lithography process (details in Table II) begins with spin coating a poly(methyl methacrylate) (PMMA) resist layer, followed by the application of a conductive coating. The resonators are patterned using a 50 kV *e*-beam lithography system, followed by the removal of the conductive layer and the development of the resist pattern.

Subsequently, the wafer is transferred to a UHV Plassys *e*-beam evaporator, where it undergoes plasma cleaning, an Ar/O_2 descum process. Titanium is then evaporated as a getter material to improve vacuum conditions, with the shutter kept closed during this step. The grAl layer is deposited at room temperature using *e*-beam evaporation of pure aluminum while a small amount of oxygen flows through the chamber. After deposition, the grAl film is lifted off by dissolving the resist underneath it. The resistivity of the resulting grAl films ranges from 800 to 2500 µΩ cm, as determined by comparing the frequencies extracted from HFSS simulation with the measured ones. SEM images of representative devices are shown in Fig. 8.

Fabrication of the CPW starts with resist spin coating, UV lithography patterning, and development. CPW

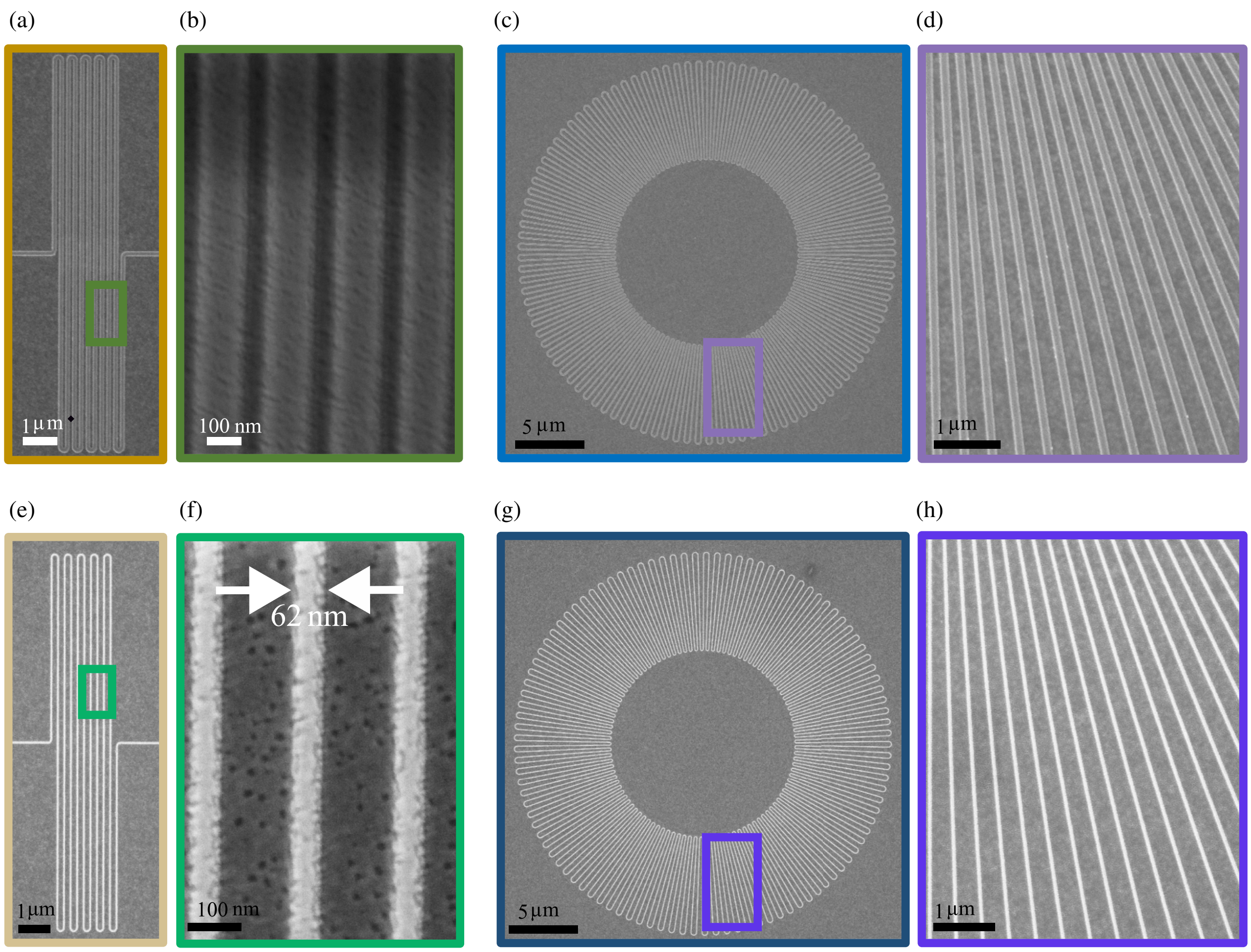

FIG. 8. Packed and narrow meandering grAl lines. SEM images of grAl meandering lines with a thickness of 30 nm, patterned using electron-beam lithography. (a),(b) Test structures with meandering lines matching the width of those in ring resonators. These simpler designs were used to optimize the fabrication recipe, achieving a packing density with a pitch of 200 nm. (c),(d) Ring resonators fabricated with the same packing density as the test structures, showing results over longer lines with a greater number of meanders. (e),(f) Test structures highlighting the minimum reproducible line width of about 60 nm. (g),(h) Ring resonators incorporate the same narrow lines as the test structures, indicating the possibility of making narrow widths in more complex geometries.

TABLE III. A summary of fabrication details for the CPW and silver ground plane, including resist spinning, UV lithography for patterning, plasma cleaning, and Nb + Al metallization. Silver ground plane is deposited using an additional optical lithography step with an Ar cleaning stage to remove Al oxide, ensuring galvanic contact between overlapping silver and Nb + Al structures.

Resist coating	
Substrate	*c*-Plane sapphire
Photoresist	AZ 5214E
Acceleration	$2000\,\mathrm{rpm\,s^{-1}}$
Spin speed	4000 rpm for 60 s
Baking temperature	110 °C for 50 s
UV exposure	
First exposure	
Exposure power	2 mW for 12 s
Baking	
Baking temperature	120 °C for 60 s
Second exposure	
Exposure type	Flood exposure for 30 s
Development	
Developer	AZ developer 3 : 2 water for 30 s
Deposition process	
Plasma cleaning	
Mass flows	O_2/Ar (10 sccm/5 sccm)
Beam parameters	$U_{\mathrm{beam}} = 200\,\mathrm{V}$, $I_{\mathrm{beam}} = 10\,\mathrm{mA}$
Gettering	
Ti evaporation rate	$0.2\,\mathrm{nm\,s^{-1}}$ for 2 min
Nb + Al deposition	
Nb evaporation rate	$1\,\mathrm{nm\,s^{-1}}$
Al evaporation rate	$1\,\mathrm{nm\,s^{-1}}$
Ag deposition	
Ag evaporation rate	$1\,\mathrm{nm\,s^{-1}}$

metallization involves Al + Nb deposition using the Plassys evaporator, including Ar/O_2 descum cleaning and Ti gettering, followed by lift-off.

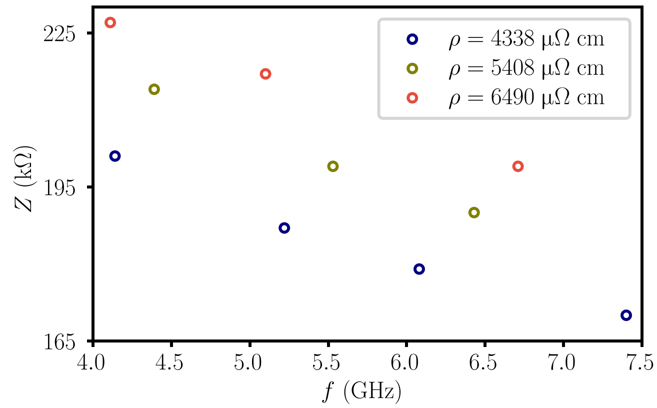

FIG. 9. Prospective grAl impedance optimization. Simulated impedances up to the fundamental mode, indicated by the x axis, for the designs summarized in Table IV.

After the CPW lift-off process, an additional optical lithography step is performed to deposit the silver ground plane. This step mirrors the CPW fabrication process but includes an additional Ar cleaning step to remove any oxide layer on Al, ensuring good galvanic contact between the overlapping silver and Nb + Al structures, which is crucial for avoiding parasitic modes. (Fabrication steps are outlined in Table III.)

After completing the patterning, a protective photoresist layer is applied, and the chip is diced into pieces of $6 \times 6\,\mathrm{mm}^2$. The final step involves cleaning off the protective resist layer.

APPENDIX E: NUMERICAL SIMULATION OF HIGH-RESISTIVITY RING RESONATORS

To explore the higher-resistivity regime of grAl below the superconducting-to-insulator phase transition (SIT), we simulated grAl ring resonators with $L_\square$ ranging from 1200 to 1800 pH/sq, which could be achieved by using ρ from 4338 to $6490\,\mu\Omega\,\mathrm{cm}$. These simulations are

TABLE IV. A summary of simulated ring resonator parameters, including geometrical dimensions, $L_\square$, L, Z, and f_0. The parameters were derived using eigenmode simulations in HFSS, focusing on the higher-resistivity regime of grAl below SIT. These results provide guidelines for designing resonators within the 4–8 GHz frequency range by optimizing impedance and frequency characteristics.

Resonator	r_{in} (μm)	w (nm)	l (μm)	p (nm)	t (nm)	f_0 (GHz)	$L_\square$ (pH/□)	L (μH)	C (fF)	Z (kΩ)
23	3.2	120	367	200	20	7.3	1200	3.67	0.518	170
24	3.69	120	469.8	200	20	6.07	1200	4.69	0.586	179
25	4.07	120	571.9	200	20	5.22	1200	5.71	0.651	187
26	4.77	120	775.7	200	20	4.14	1200	7.75	0.763	201
27	3.31	120	377	200	20	6.43	1500	4.7	0.521	190
28	3.62	120	459	200	20	5.53	1500	5.7	0.581	199
29	4.2	120	622	200	20	4.39	1500	7.7	0.683	214
30	2.9	120	316	200	20	6.7	1800	4.7	0.480	199
31	3.6	120	452	200	20	5.09	1800	6.7	0.584	217
32	4.13	120	588	200	20	4.1	1800	8.8	0.685	227

performed using the eigenmode solver in ANSYS HFSS to determine intrinsic resonant frequencies.

The simulated parameters, including resonator dimensions, inductance, resonance frequencies, and corresponding impedances, are presented in Table IV, and the impedance values are reported in Fig. 9, providing a perspective for future impedance increases in grAl resonators.

[1] M. Devoret, S. Girvin, and R. Schoelkopf, Circuit-QED: How strong can the coupling between a Josephson junction atom and a transmission line resonator be? Ann. Phys. **519**, 767 (2007).

[2] G. Burkard, T. D. Ladd, A. Pan, J. M. Nichol, and J. R. Petta, Semiconductor spin qubits, Rev. Mod. Phys. **95**, 025003 (2023).

[3] P. Arrangoiz-Arriola, E. A. Wollack, M. Pechal, J. D. Witmer, J. T. Hill, and A. H. Safavi-Naeini, Coupling a superconducting quantum circuit to a phononic crystal defect cavity, Phys. Rev. X **8**, 031007 (2018).

[4] A. Bozkurt, H. Zhao, C. Joshi, H. G. LeDuc, P. K. Day, and M. Mirhosseini, A quantum electromechanical interface for long-lived phonons, Nat. Phys. **19**, 1326 (2023).

[5] A. André, D. DeMille, J. M. Doyle, M. D. Lukin, S. E. Maxwell, P. Rabl, R. J. Schoelkopf, and P. Zoller, A coherent all-electrical interface between polar molecules and mesoscopic superconducting resonators, Nat. Phys. **2**, 636 (2006).

[6] V. E. Manucharyan, N. A. Masluk, A. Kamal, J. Koch, L. I. Glazman, and M. H. Devoret, Evidence for coherent quantum phase slips across a Josephson junction array, Phys. Rev. B **85**, 024521 (2012).

[7] N. A. Masluk, I. M. Pop, A. Kamal, Z. K. Minev, and M. H. Devoret, Microwave characterization of Josephson junction arrays: Implementing a low loss superinductance, Phys. Rev. Lett. **109**, 137002 (2012).

[8] V. E. Manucharyan, J. Koch, L. I. Glazman, and M. H. Devoret, Fluxonium: Single Cooper-pair circuit free of charge offsets, Science **326**, 113 (2009).

[9] I. M. Pop, K. Geerlings, G. Catelani, R. J. Schoelkopf, L. I. Glazman, and M. H. Devoret, Coherent suppression of electromagnetic dissipation due to superconducting quasiparticles, Nature **508**, 369 (2014).

[10] L. Grünhaupt, M. Spiecker, D. Gusenkova, N. Maleeva, S. T. Skacel, I. Takmakov, F. Valenti, P. Winkel, H. Rotzinger, W. Wernsdorfer, A. V. Ustinov, and I. M. Pop, Granular aluminium as a superconducting material for high-impedance quantum circuits, Nat. Mater. **18**, 816 (2019).

[11] M. Pita-Vidal, A. Bargerbos, C.-K. Yang, D. J. Van Woerkom, W. Pfaff, N. Haider, P. Krogstrup, L. P. Kouwenhoven, G. De Lange, and A. Kou, Gate-tunable field-compatible fluxonium, Phys. Rev. Appl. **14**, 064038 (2020).

[12] L. B. Nguyen, G. Koolstra, Y. Kim, A. Morvan, T. Chistolini, S. Singh, K. N. Nesterov, C. Jünger, L. Chen, Z. Pedramrazi, B. K. Mitchell, J. M. Kreikebaum, S. Puri, D. I. Santiago, and I. Siddiqi, Blueprint for a high-performance fluxonium quantum processor, PRX Quantum **3**, 037001 (2022).

[13] M. Peruzzo, F. Hassani, G. Szep, A. Trioni, E. Redchenko, M. Žemlička, and J. M. Fink, Geometric superinductance qubits: Controlling phase delocalization across a single Josephson junction, PRX Quantum **2**, 040341 (2021).

[14] K. Kalashnikov, W. T. Hsieh, W. Zhang, W.-S. Lu, P. Kamenov, A. Di Paolo, A. Blais, M. E. Gershenson, and M. Bell, Bifluxon: Fluxon-parity-protected superconducting qubit, PRX Quantum **1**, 010307 (2020).

[15] P. Brooks, A. Kitaev, and J. Preskill, Protected gates for superconducting qubits, Phys. Rev. A **87**, 052306 (2013).

[16] P. Groszkowski, A. D. Paolo, A. L. Grimsmo, A. Blais, D. I. Schuster, A. A. Houck, and J. Koch, Coherence properties of the 0-π qubit, New J. Phys. **20**, 043053 (2018).

[17] A. Gyenis, P. S. Mundada, A. Di Paolo, T. M. Hazard, X. You, D. I. Schuster, J. Koch, A. Blais, and A. A. Houck, Experimental realization of a protected superconducting circuit derived from the 0–π qubit, PRX Quantum **2**, 010339 (2021).

[18] R. S. Shaikhaidarov, K. H. Kim, J. W. Dunstan, I. V. Antonov, S. Linzen, M. Ziegler, D. S. Golubev, V. N. Antonov, E. V. Il'ichev, and O. V. Astafiev, Quantized current steps due to the a.c. coherent quantum phase-slip effect, Nature **608**, 45 (2022).

[19] N. Crescini, S. Cailleaux, W. Guichard, C. Naud, O. Buisson, K. W. Murch, and N. Roch, Evidence of dual Shapiro steps in a Josephson junction array, Nat. Phys. **19**, 851 (2023).

[20] F. Kaap, C. Kissling, V. Gaydamachenko, L. Grünhaupt, and S. Lotkhov, Demonstration of dual Shapiro steps in small Josephson junctions, Nat. Commun. **15**, 8726 (2024).

[21] I. V. Pechenezhskiy, R. A. Mencia, L. B. Nguyen, Y.-H. Lin, and V. E. Manucharyan, The superconducting quasicharge qubit, Nature **585**, 368 (2020).

[22] C. Jünger, T. Chistolini, L. B. Nguyen, H. Kim, L. Chen, T. Ersevim, W. Livingston, G. Koolstra, D. I. Santiago, and I. Siddiqi, Implementation of scalable suspended superinductors, Appl. Phys. Lett. **126**, 044003 (2025).

[23] S. Frasca, I. Arabadzhiev, S. B. De Puechredon, F. Oppliger, V. Jouanny, R. Musio, M. Scigliuzzo, F. Minganti, P. Scarlino, and E. Charbon, NbN films with high kinetic inductance for high-quality compact superconducting resonators, Phys. Rev. Appl. **20**, 044021 (2023).

[24] M. Peruzzo, A. Trioni, F. Hassani, M. Zemlicka, and J. M. Fink, Surpassing the resistance quantum with a geometric superinductor, Phys. Rev. Appl. **14**, 044055 (2020).

[25] M. Medahinne, Y. P. Kandel, S. T. Magar, E. Champion, J. M. Nichol, and M. S. Blok, Magnetic-field-tolerant superconducting spiral resonators for circuit quantum electrodynamics, Phys. Rev. Appl. **23**, 014070 (2025).

[26] M. Pita-Vidal, J. J. Wesdorp, L. J. Splitthoff, A. Bargerbos, Y. Liu, L. P. Kouwenhoven, and C. K. Andersen, Strong tunable coupling between two distant superconducting spin qubits, Nat. Phys. **20**, 1158 (2024).

[27] T. W. Larsen, K. D. Petersson, F. Kuemmeth, T. S. Jespersen, P. Krogstrup, J. Nygård, and C. M. Marcus, Semiconductor-nanowire-based superconducting qubit, Phys. Rev. Lett. **115**, 127001 (2015).

[28] M. Valentini, F. Peñaranda, A. Hofmann, M. Brauns, R. Hauschild, P. Krogstrup, P. San-Jose, E. Prada, R. Aguado,

and G. Katsaros, Nontopological zero-bias peaks in full-shell nanowires induced by flux-tunable Andreev states, Science **373**, 82 (2021).

[29] F. Luthi, T. Stavenga, O. W. Enzing, A. Bruno, C. Dickel, N. K. Langford, M. A. Rol, T. S. Jespersen, J. Nygård, P. Krogstrup, and L. DiCarlo, Evolution of nanowire transmon qubits and their coherence in a magnetic field, Phys. Rev. Lett. **120**, 100502 (2018).

[30] D. Niepce, J. Burnett, and J. Bylander, High kinetic inductance NbN nanowire superinductors, Phys. Rev. Appl. **11**, 044014 (2019).

[31] M. Yang, X. He, W. Gao, J. Chen, Y. Wu, X. Wang, G. Mu, W. Peng, and Z. Lin, Kinetic inductance compact resonator with NbTiN micronwires, AIP Adv. **14**, 085027 (2024).

[32] A. Shearrow, G. Koolstra, S. J. Whiteley, N. Earnest, P. S. Barry, F. J. Heremans, D. D. Awschalom, E. Shirokoff, and D. I. Schuster, Atomic layer deposition of titanium nitride for quantum circuits, Appl. Phys. Lett. **113**, 212601 (2018).

[33] K. R. Amin, C. Ladner, G. Jourdan, S. Hentz, N. Roch, and J. Renard, Loss mechanisms in tin high impedance superconducting microwave circuits, Appl. Phys. Lett. **120**, 164001 (2022).

[34] M. R. Vissers, J. Gao, D. S. Wisbey, D. A. Hite, C. C. Tsuei, A. D. Corcoles, M. Steffen, and D. P. Pappas, Low loss superconducting titanium nitride coplanar waveguide resonators, Appl. Phys. Lett. **97**, 232509 (2010).

[35] N. Samkharadze, A. Bruno, P. Scarlino, G. Zheng, D. P. DiVincenzo, L. DiCarlo, and L. M. K. Vandersypen, High-kinetic-inductance superconducting nanowire resonators for circuit QED in a magnetic field, Phys. Rev. Appl. **5**, 044004 (2016).

[36] J. G. Kroll, F. Borsoi, K. L. Van Der Enden, W. Uilhoorn, D. De Jong, M. Quintero-Pérez, D. J. Van Woerkom, A. Bruno, S. R. Plissard, D. Car, E. P. A. M. Bakkers, M. C. Cassidy, and L. P. Kouwenhoven, Magnetic-field-resilient superconducting coplanar-waveguide resonators for hybrid circuit quantum electrodynamics experiments, Phys. Rev. Appl. **11**, 064053 (2019).

[37] M. Müller, T. Luschmann, A. Faltermeier, S. Weichselbaumer, L. Koch, G. B. P. Huber, H. W. Schumacher, N. Ubbelohde, D. Reifert, T. Scheller, F. Deppe, A. Marx, S. Filipp, M. Althammer, R. Gross, and H. Huebl, Magnetic field robust high quality factor NbTiN superconducting microwave resonators, Mater. Quantum. Technol. **2**, 015002 (2022).

[38] R. Gao, H. Ku, H. Deng, W. Yu, T. Xia, F. Wu, Z. Song, M. Wang, X. Miao, C. Zhang, Y. Lin, Y. Shi, H. Zhao, and C. Deng, Ultrahigh kinetic inductance superconducting materials from spinodal decomposition, Adv. Mater. **34**, 2201268 (2022).

[39] H. Rotzinger, S. T. Skacel, M. Pfirrmann, J. N. Voss, J. Münzberg, S. Probst, P. Bushev, M. P. Weides, A. V. Ustinov, and J. E. Mooij, Aluminium-oxide wires for superconducting high kinetic inductance circuits, Supercond. Sci. Technol. **30**, 025002 (2016).

[40] P. Kamenov, W.-S. Lu, K. Kalashnikov, T. DiNapoli, M. T. Bell, and M. E. Gershenson, Granular aluminum meandered superinductors for quantum circuits, Phys. Rev. Appl. **13**, 054051 (2020).

[41] M. Janík, K. Roux, C. B. Espinosa, O. Sagi, A. Baghdadi, T. Adletzberger, S. Calcaterra, M. Botifoll, A. G. Manjón, J. Arbiol, D. Chrastina, G. Isella, I. M. Pop, and G. Katsaros, Strong charge-photon coupling in planar germanium enabled by granular aluminium superinductors, Nat. Commun. **16**, 2103 (2025).

[42] V. Gupta, P. Winkel, N. Thakur, P. van Vlaanderen, Y. Wang, S. Ganjam, L. Frunzio, and R. J. Schoelkopf, Low loss lumped-element inductors made from granular aluminum, Phys. Rev. Appl. **23**, 054067 (2025).

[43] M. Xu, R. Cheng, Y. Wu, G. Liu, and H. X. Tang, Magnetic field-resilient quantum-limited parametric amplifier, PRX Quantum **4**, 010322 (2023).

[44] C. Joshi, W. Chen, H. G. LeDuc, P. K. Day, and M. Mirhosseini, Strong kinetic-inductance kerr nonlinearity with titanium nitride nanowires, Phys. Rev. Appl. **18**, 064088 (2022).

[45] N. Maleeva, L. Grünhaupt, T. Klein, F. Levy-Bertrand, O. Dupre, M. Calvo, F. Valenti, P. Winkel, F. Friedrich, W. Wernsdorfer, A. V. Ustinov, H. Rotzinger, A. Monfardini, M. V. Fistul, and I. M. Pop, Circuit quantum electrodynamics of granular aluminum resonators, Nat. Commun. **9**, 3889 (2018).

[46] P. Winkel, K. Borisov, L. Grünhaupt, D. Rieger, M. Spiecker, F. Valenti, A. V. Ustinov, W. Wernsdorfer, and I. M. Pop, Implementation of a transmon qubit using superconducting granular aluminum, Phys. Rev. X **10**, 031032 (2020).

[47] C. Roy, S. Frasca, and P. Scarlino, Study of magnetic field resilient high impedance high-kinetic inductance superconducting resonators, arXiv:2503.13321.

[48] F. Levy-Bertrand, T. Klein, T. Grenet, O. Dupré, A. Benoît, A. Bideaud, O. Bourrion, M. Calvo, A. Catalano, A. Gomez, J. Goupy, L. Grünhaupt, U. V. Luepke, N. Maleeva, F. Valenti, I. M. Pop, and A. Monfardini, Electrodynamics of granular aluminum from superconductor to insulator: Observation of collective superconducting modes, Phys. Rev. B **99**, 094506 (2019).

[49] M. Tinkham, *Introduction to Superconductivity* (Dover Publications, Mineola, 2004).

[50] A. J. Annunziata, D. F. Santavicca, L. Frunzio, G. Catelani, M. J. Rooks, A. Frydman, and D. E. Prober, Tunable superconducting nanoinductors, Nanotechnology **21**, 445202 (2010).

[51] Z. K. Minev, I. M. Pop, and M. H. Devoret, Planar superconducting whispering gallery mode resonators, Appl. Phys. Lett. **103**, 142604 (2013).

[52] U. S. Pracht, N. Bachar, L. Benfatto, G. Deutscher, E. Farber, M. Dressel, and M. Scheffler, Enhanced Cooper pairing versus suppressed phase coherence shaping the superconducting dome in coupled aluminum nanograins, Phys. Rev. B **93**, 100503 (2016).

[53] F. Henriques, F. Valenti, T. Charpentier, M. Lagoin, C. Gouriou, M. Martínez, L. Cardani, M. Vignati, L. Grünhaupt, D. Gusenkova, J. Ferrero, S. T. Skacel, W. Wernsdorfer, A. V. Ustinov, G. Catelani, O. Sander, and I. M. Pop, Phonon traps reduce the quasiparticle density in superconducting circuits, Appl. Phys. Lett. **115**, 212601 (2019).

[54] L. Grünhaupt, U. Von Lüpke, D. Gusenkova, S. T. Skacel, N. Maleeva, S. Schlör, A. Bilmes, H. Rotzinger, A. V. Ustinov, M. Weides, and I. M. Pop, An argon ion beam milling process for native AlO_x layers enabling coherent

superconducting contacts, Phys. Rev. Appl. **111**, 072601 (2017).

[55] M. S. Bartlett, Smoothing periodograms from time-series with continuous spectra, Nature **161**, 686 (1948).

[56] F. Valenti, F. Henriques, G. Catelani, N. Maleeva, L. Grünhaupt, U. Von Lüpke, S. T. Skacel, P. Winkel, A. Bilmes, A. V. Ustinov, J. Goupy, M. Calvo, A. Benoît, F. Levy-Bertrand, A. Monfardini, and I. M. Pop, Interplay between kinetic inductance, nonlinearity, and quasiparticle dynamics in granular aluminum microwave kinetic inductance detectors, Phys. Rev. Appl. **11**, 054087 (2019).

[57] J. Burnett, A. Bengtsson, D. Niepce, and J. Bylander, Noise and loss of superconducting aluminium resonators at single photon energies, J. Phys. Conf. Ser. **969**, 012131 (2018).

[58] S. Schlör, J. Lisenfeld, C. Müller, A. Bilmes, A. Schneider, D. P. Pappas, A. V. Ustinov, and M. Weides, Correlating decoherence in transmon qubits: Low frequency noise by single fluctuators, Phys. Rev. Lett. **123**, 190502 (2019).

[59] M. Kristen, J. N. Voss, M. Wildermuth, H. Rotzinger, and A. V. Ustinov, Random telegraph fluctuations in granular microwave resonators, Appl. Phys. Lett. **122**, 202602 (2023).

[60] D. Rieger, S. Günzler, M. Spiecker, A. Nambisan, W. Wernsdorfer, and I. M. Pop, Fano interference in microwave resonator measurements, Phys. Rev. Appl. **20**, 014059 (2023).

[61] L. Grünhaupt, N. Maleeva, S. T. Skacel, M. Calvo, F. Levy-Bertrand, A. V. Ustinov, H. Rotzinger, A. Monfardini, G. Catelani, and I. M. Pop, Loss mechanisms and quasiparticle dynamics in superconducting microwave resonators made of thin-film granular aluminum, Phys. Rev. Lett. **121**, 117001 (2018).

[62] S. Hunklinger, W. Arnold, S. Stein, R. Nava, and K. Dransfeld, Saturation of the ultrasonic absorption in vitreous silica at low temperatures, Phys. Lett. A **42**, 253 (1972).

[63] B. Golding, J. E. Graebner, B. I. Halperin, and R. J. Schutz, Nonlinear phonon propagation in fused silica below 1 K, Phys. Rev. Lett. **30**, 223 (1973).

[64] E. M. Levenson-Falk, F. Kos, R. Vijay, L. Glazman, and I. Siddiqi, Single-quasiparticle trapping in aluminum nanobridge Josephson junctions, Phys. Rev. Lett. **112**, 047002 (2014).

[65] S. Gustavsson, F. Yan, G. Catelani, J. Bylander, A. Kamal, J. Birenbaum, D. Hover, D. Rosenberg, G. Samach, A. P. Sears, S. J. Weber, J. L. Yoder, J. Clarke, A. J. Kerman, F. Yoshihara, Y. Nakamura, T. P. Orlando, and W. D. Oliver, Suppressing relaxation in superconducting qubits by quasiparticle pumping, Science **354**, 1573 (2016).

[66] H. Jin, G. Serpico, Y. Lee, T. Confalone, C. N. Saggau, F. Lo Sardo, G. Gu, B. H. Goodge, E. Lesne, D. Montemurro, K. Nielsch, N. Poccia, and U. Vool, Exploring van der Waals cuprate superconductors using a hybrid microwave circuit, Nano Lett. **25**, 3191 (2025).

[67] G. Andersson, A. L. O. Bilobran, M. Scigliuzzo, M. M. de Lima, J. H. Cole, and P. Delsing, Acoustic spectral hole-burning in a two-level system ensemble, npj Quantum Inf. **7**, 1 (2021).

[68] T. Capelle, E. Flurin, E. Ivanov, J. Palomo, M. Rosticher, S. Chua, T. Briant, P.-F. Cohadon, A. Heidmann, T. Jacqmin, and S. Deléglise, Probing a two-level system bath via the frequency shift of an off-resonantly driven cavity, Phys. Rev. Appl. **13**, 034022 (2020).

[69] N. Kirsh, E. Svetitsky, A. L. Burin, M. Schechter, and N. Katz, Revealing the nonlinear response of a tunneling two-level system ensemble using coupled modes, Phys. Rev. Mater. **1**, 012601 (2017).

[70] M. Khorramshahi, ZENODO, 2024, http://doi.org/10.5281/zenodo.16566910.

[71] F. R. Zypman, Mathematical expression for the capacitance of coplanar strips, J. Electrostat. **101**, 103371 (2019).